







# The edge of the Galaxy

Alis J. Deason ,<sup>1</sup>★ Azadeh Fattahi ,<sup>1</sup> Carlos S. Frenk,<sup>1</sup> Robert J. J. Grand ,<sup>2</sup>  
 Kyle A. Oman ,<sup>1</sup> Shea Garrison-Kimmel ,<sup>3</sup> Christine M. Simpson ,<sup>4,5</sup>  
 and Julio F. Navarro<sup>6</sup>

<sup>1</sup>*Institute for Computational Cosmology, Department of Physics, University of Durham, South Road, Durham DH1 3LE, UK*

<sup>2</sup>*Max-Planck-Institut für Astrophysik, Karl-Schwarzschild-Str. 1, D-85748 Garching, Germany*

<sup>3</sup>*Factual Inc., 1999 Ave of the Stars, Los Angeles, CA 90067, USA*

<sup>4</sup>*Enrico Fermi Institute, The University of Chicago, Chicago, IL 60637, USA*

<sup>5</sup>*Department of Astronomy and Astrophysics, and Kavli Institute for Cosmological Physics, The University of Chicago, Chicago, IL 60637, USA*

<sup>6</sup>*Department of Physics and Astronomy, University of Victoria, PO Box 3055 STN CSC, Victoria, BC V8W 3P6, Canada*

Accepted 2020 June 10. Received 2020 May 22; in original form 2020 February 21

## ABSTRACT

We use cosmological simulations of isolated Milky Way (MW)-mass galaxies, as well as Local Group (LG) analogues, to define the ‘edge’ – a caustic manifested in a drop in density or radial velocity – of Galactic-sized haloes, both in dark matter and in stars. In the dark matter, we typically identify two caustics: the outermost caustic located at  $\sim 1.4r_{200m}$ , corresponding to the ‘splashback’ radius, and a second caustic located at  $\sim 0.6r_{200m}$ , which likely corresponds to the edge of the virialized material that has completed at least two pericentric passages. The splashback radius is ill defined in LG-type environments where the haloes of the two galaxies overlap. However, the second caustic is less affected by the presence of a companion, and is a more useful definition for the boundary of the MW halo. Curiously, the stellar distribution also has a clearly defined caustic, which, in most cases, coincides with the second caustic of the dark matter. This can be identified in both radial density and radial velocity profiles, and should be measurable in future observational programmes. Finally, we show that the second caustic can also be identified in the phase-space distribution of dwarf galaxies in the LG. Using the current dwarf galaxy population, we predict the edge of the MW halo to be  $292 \pm 61$  kpc.

**Key words:** methods: numerical – Galaxy: halo – galaxies: haloes – galaxies: kinematics and dynamics – Local Group.

## 1 INTRODUCTION

The mass condensations commonly referred to as dark matter haloes in simulations fade gradually into the background matter distribution and have no well-defined edge (e.g. Diemer, More & Kravtsov 2013). Furthermore, haloes are not spherical but have irregular shapes. Nevertheless, definitions of the nominal boundary of a halo such as the ‘friends-of-friends’ radius (Davis et al. 1985), the ‘virial radius’ (e.g. Cole & Lacey 1996), or ‘ $r_{200}$ ’ abound in the literature. Even the latter is ambiguous, as it is sometimes defined as the radius,  $r_{200c}$ , within which the mean density equals 200 times the critical density (e.g. Navarro, Frenk & White 1996) or as the radius,  $r_{200m}$ , within which the mean density equals 200 times the mean cosmic value (e.g. Diemand, Kuhlen & Madau 2007).

From a practical point of view, the ambiguity regarding the definition of the boundary of a dark matter halo can become

troublesome when we want to define the dark matter particles, stars, gas, or subhaloes that ‘belong’ to a halo, or when we wish to define the radius at which tracers can escape from a self-bound system (e.g. Leonard & Tremaine 1990; Springel 2005). The physical extent of haloes varies significantly at different mass scales and in different environments (e.g. Navarro et al. 1996; Navarro, Frenk & White 1997; Bullock et al. 2001; Wechsler et al. 2002) and, when contrasting simulations or comparing them to observations, a common definition of halo extent is essential to avoid confusion. In addition, while the backdrop of our current theory of structure formation is cold dark matter, it is just as important to understand how the baryonic components relate to the dark matter, and where observational boundaries lie (e.g. Kravtsov 2013; Shull 2014; Wechsler & Tinker 2018).

Analytical solutions for the collapse of spherical gravitational structures in a cosmological context provide valuable insight into the structure of dark matter haloes. The spherical collapse model, first presented by Gunn & Gott (1972) for an Einstein–de Sitter Universe, describes the evolution of spherical shells of matter around an

\* E-mail: [alis.j.deason@durham.ac.uk](mailto:alis.j.deason@durham.ac.uk)

overdensity (see also Fillmore & Goldreich 1984; Bertschinger 1985). In this model, initially overdense regions gravitationally attract the surrounding matter, causing it to detach from the Hubble flow and collapse, forming larger and larger equilibrium structures. Each successive mass shell collapses on to a deeper potential well and thus has a higher energy and a larger apocentre. Material piles up at these apocentres, giving rise to a singularity or caustic surface. Of particular interest is the outermost caustic, termed the ‘splashback’ radius, which corresponds to the apocentre of material that has most recently completed its first pericentric passage.

The spherical collapse model has served as a motivation for many of the commonly used definitions of halo masses and sizes. Traditionally (see e.g. Binney & Tremaine 2008, section 9.2.1), an Einstein–de Sitter Universe is assumed, where energy conservation and the virial theorem imply that the ‘virial’ radius (enclosing the mass whose potential energy is twice the negative kinetic energy) occurs at half the turnaround radius. In the Einstein–de Sitter model, the overdensity (relative to the critical density) at virialization is  $\Delta_c = \rho_{\text{vir}}/\rho_c = 18\pi^2 = 178$ . This formalism has been generalized for a Lambda cold dark matter ( $\Lambda$ CDM) universe (Lahav et al. 1991; Bryan & Norman 1998; Eke, Navarro & Frenk 1998), in which case the overdensity defining the boundary is  $\Delta_c \sim 100$  at  $z = 0$ , and evolves with redshift.

In the spherical collapse model, the virial radius defines the region within which the system is virialized; beyond this radius, mass is still collapsing on to the object.  $N$ -body simulations suggest that this distinction occurs at  $\Delta_c \sim 200$  (Cole & Lacey 1996), so a commonly used definition of halo is  $r_{200c}$ . Another commonly used definition, particularly in studies of the halo occupation distribution of galaxies (e.g. Berlind & Weinberg 2002; Kravtsov et al. 2004), is  $r_{200m}$ , which corresponds to  $\Delta_c = 200 \times \Omega_m \sim 60$  today. For a Milky Way (MW)-mass halo ( $\sim 1 \times 10^{12} M_\odot$ ), these halo boundaries are typically  $r_{200c} \approx 220$ ,  $r_{\text{vir}} \approx 290$ , and  $r_{200m} \approx 350$  kpc. Several authors have argued that the splashback radius, predicted by the spherical collapse model, is the most natural definition of the boundary of a halo (e.g. Adhikari, Dalal & Chamberlain 2014; Diemer & Kravtsov 2014; More, Diemer & Kravtsov 2015). For a MW halo, the splashback radius is typically  $\sim 500$  kpc (assuming the splashback radius lies at  $\sim 1.5r_{200m}$ , see below).

In reality, halo collapse is non-spherical, lumpy, and significantly anisotropic. Several works have used  $N$ -body simulations to follow this collapse in detail (e.g. Davis et al. 1985; Frenk et al. 1988; Cole & Lacey 1996; Diemand & Kuhlen 2008; Springel et al. 2008) and to compare with the predictions of the spherical collapse model (e.g. Prada et al. 2006; Ascasibar, Hoffman & Gottlöber 2007; Zavala, Okamoto & Frenk 2008; Ludlow et al. 2010). While most studies have concentrated on the inner profiles of dark matter haloes (e.g. Navarro et al. 1996; Moore et al. 1999a; Stadel et al. 2009), more recently, Adhikari et al. (2014), Diemer & Kravtsov (2014), and More et al. (2015) have explored the outer density profiles of dark matter haloes. These studies identify the outer caustic, or splashback radius, as a sharp jump in the density profile. For example, Diemer & Kravtsov (2014) and More et al. (2015) find that the splashback radius falls in the range  $(0.8\text{--}1.0)r_{200m}$  for rapidly accreting haloes, and is  $\approx 1.5r_{200m}$  for slowly accreting haloes.

The influence of environment, mass accretion rate, and redshift on the splashback radius was investigated by Diemer et al. (2017) and Mansfield, Kravtsov & Diemer (2017) and the splashback radius is now a commonly used, and thoroughly explored, halo boundary. Interestingly, there is now considerable evidence that splashback radii have been measured observationally in the outskirts of galaxy clusters (e.g. More et al. 2016; Baxter et al. 2017; Chang et al. 2018;

Contigiani, Hoekstra & Bahé 2019; Shin et al. 2019; Zürcher & More 2019; Murata et al. 2020). While the measured splashback radii tend to be smaller than those predicted in  $\Lambda$ CDM simulations, these results are still subject to systematic effects (Busch & White 2017; Xhakaj et al. 2019; Murata et al. 2020).

Often, the most relevant, and even the most physical, definition of halo boundary depends on the situation at hand. The term splashback is often used by reference to the population of ‘backsplash’ galaxies, i.e. galaxies that have been inside, but are now outside the virial radius, and may extend well beyond any traditional spherical collapse boundary (e.g. Balogh, Navarro & Morris 2000; Mamon et al. 2004; Gill, Knebe & Gibson 2005; Sales et al. 2007; Ludlow et al. 2009; Teyssier, Johnston & Kuhlen 2012; Bahé et al. 2013; Wetzel et al. 2014). The properties of these backsplash galaxies demonstrate that the environmental effects of haloes can extend well beyond the traditional virial radius boundary. However, even if the zone of influence of haloes extends significantly beyond the virial radius, haloes are never isolated systems, and eventually run into other massive systems. For example, the MW galaxy resides in the Local Group (LG), and is located  $\sim 800$  kpc from the roughly equal mass halo of M31. Thus, the splashback radius for a MW-mass halo runs into that of M31. In this case, it is perhaps more physical to consider the splashback radius of the entire LG, rather than of its individual components. Nonetheless, a physically motivated definition of the extent for the MW is warranted, and will become even more important when the next-generation surveys discover many tens of dwarf galaxies in the LG.

In this work, we explore the boundary of MW-mass haloes using high-resolution cosmological simulations. In particular, we use the outer density profiles of the haloes to quantify their extent. We take into account two important characteristics of the MW: (1) its location in the LG, and hence its proximity to M31, and (2) the relation between the extent of the stellar distribution and that of the underlying dark matter. This consideration is important for observational probes of the MW halo boundary. In Section 2, we describe the cosmological simulations used in this work. These comprise both collisionless and hydrodynamic simulations, as well as simulations designed to mimic the LG. We quantify the ‘edges’ of the dark matter haloes, stellar haloes, and satellite dwarf galaxy populations, and compare these various boundaries in Section 3. Finally, we summarize our main results in Section 4.

## 2 SIMULATIONS

We use a large range of high-resolution simulations of MW-mass haloes to quantify the edges of Galactic-sized haloes. Below we describe each simulation suite in turn.

### 2.1 ELVIS

The ‘Exploring the Local Volume in Simulations’ (ELVIS) project is a suite of 48 simulations of Galaxy-size haloes (Garrison-Kimmel et al. 2014). These simulations were designed to model the LG environment in a cosmological context. Half of the haloes (24) are in paired configurations similar to the MW and M31. The LG analogues were selected from medium-resolution ( $m_p = 9.7 \times 10^7 M_\odot$ , force softening 1.4 kpc) cosmological simulations. Twelve halo pairs were selected for resimulation based on phase-space criteria appropriate to the MW/M31 system (e.g. separation, total mass, radial velocity). The resulting zoom simulations are high-resolution ( $m_p = 1.9 \times 10^5 M_\odot$ , force softening 141 pc) volumes that span 2–5 Mpc in size. The remaining half (24) of

the ELVIS suite are isolated, mass-matched analogues, which are resimulated at the same resolution as the paired haloes. The resulting sample consists of 48 high-resolution haloes in the mass range  $(1-3) \times 10^{12} M_{\odot}$ . The ELVIS suite was run with the *WMAP-7* cosmology (Larson et al. 2011) with parameters  $\Omega_M = 0.266$ ,  $\Omega_{\Lambda} = 0.734$ , and  $H_0 = 71 \text{ km s}^{-1} \text{ Mpc}^{-1}$ .

Subhaloes were identified using the ROCKSTAR halo finder (Behroozi, Wechsler & Wu 2013a) and were followed through time with CONSISTENT TREES (Behroozi et al. 2013b). We define the centre of the host haloes using the position and velocity of the main subhalo calculated in the ROCKSTAR algorithm. Garrison-Kimmel et al. (2014) find that the subhalo sample in ELVIS is complete down to  $M_{\text{sub}} > 2 \times 10^7 M_{\odot}$  (or  $V_{\text{max}} > 8 \text{ km s}^{-1}$ ). The general properties of the ELVIS haloes are described in Garrison-Kimmel et al. (2014) and summarized in their table 1. This suite has produced a number of results, including predictions for future dwarf galaxy detections (Garrison-Kimmel et al. 2014), the stellar–mass halo relation for LG galaxies (Garrison-Kimmel et al. 2017), the prevalence of dwarf–dwarf mergers and group infall on to MW-mass haloes (Deason et al. 2014b; Wetzel, Deason & Garrison-Kimmel 2015), and insights into the planar alignment of MW satellites (Pawlowski, Ibata & Bullock 2017).

## 2.2 APOSTLE

APOSTLE (A Project Of Simulating The Local Environment) is a suite of high-resolution, hydrodynamic simulations consisting of 12 halo pairs (Fattahi et al. 2016; Sawala et al. 2016). These pairs were drawn from the medium-resolution ( $m_p = 8.8 \times 10^6 M_{\odot}$ ) DOVE dark-matter-only cosmological simulation described by Jenkins (2013). The candidates were selected to have paired configurations similar to the LG, based on the separation of the pairs, their relative radial and tangential velocities, a Hubble flow constraint, and the combined mass of the pair. The exact selection criteria differ from the ELVIS suite, with the main difference being the total masses of the haloes. The APOSTLE suite has typically lower halo masses, and span the mass range  $(0.5-2.5) \times 10^{12} M_{\odot}$ . The resimulations span 2–3 Mpc in size and were run with the same hydrodynamic code as the EAGLE Reference calibration (Crain et al. 2015; Schaye et al. 2015), which includes subgrid prescriptions for star formation, feedback, metal enrichment, cosmic reionization, and active galactic nuclei. The simulations were performed at three different resolution levels, and we use the ‘medium’ L2 resolution suite that has 10 times better mass resolution than DOVE ( $m_p = 6 \times 10^5 M_{\odot}$ , force softening 307 pc), with a gas particle mass of  $1.2 \times 10^5 M_{\odot}$ . APOSTLE was run with the *WMAP-7* cosmology (Komatsu et al. 2011) with parameters  $\Omega_M = 0.272$ ,  $\Omega_b = 0.0455$ ,  $\Omega_{\Lambda} = 0.728$ , and  $H_0 = 70.4 \text{ km s}^{-1} \text{ Mpc}^{-1}$ .

Haloes are identified using a friends-of-friends (FOF) algorithm (Davis et al. 1985), and subhaloes belonging to each FOF halo were identified using the SUBFIND algorithm (Springel et al. 2001). We use the position and velocity of the main (sub)halo calculated in SUBFIND to define the centre of the host halo. Note that this definition of halo centre is different to the one used in ELVIS, which is based on ROCKSTAR. For a comparison of the SUBFIND and ROCKSTAR subhalo finding algorithms, see e.g. Knebe et al. (2011). Sawala et al. (2016) showed that the satellite luminosity function of APOSTLE L2 is complete down to  $M_{\text{star}} \sim 10^5 M_{\odot}$ , and they used the APOSTLE suite to address apparent small-scale problems in the  $\Lambda$ CDM cosmology. In particular, they showed that the simulations match the abundance of observed dwarf satellites in the MW and M31, thus solving the apparent ‘missing satellites’ (Moore et al. 1999b)

and ‘too-big-to-fail’ (Boylan-Kolchin, Bullock & Kaplinghat 2011) problems. Several other works have used the APOSTLE suite to investigate a wide range of topics. These include probing the nature and properties of dark matter (Lovell et al. 2017; Sawala et al. 2017), the tidal stripping of dwarf galaxies and formation of the stellar halo (Starkenburger et al. 2017; Fattahi et al. 2018), and tests of observational mass estimates of dwarf galaxies (Campbell et al. 2017; Genina et al. 2018, 2019).

## 2.3 Auriga

The Auriga suite consists of cosmological hydrodynamical zoom-in simulations of isolated MW-mass haloes (Grand et al. 2017). Candidates for resimulation were selected from the 100-cMpc dark-matter-only cube of the EAGLE simulation (Schaye et al. 2015). The sample of Auriga haloes was chosen to be relatively isolated at  $z = 0$ , with no objects with masses greater than half of the parent halo closer than 1.37 Mpc. The initial sample of 30 haloes was selected in the mass range  $(1-2) \times 10^{12} M_{\odot}$ , and a further 10 lower mass  $((0.5-1) \times 10^{12} M_{\odot})$  haloes were more recently added to the suite (Grand et al. 2019b). The zoom resimulations were performed with the AREPO code, which follows magnetohydrodynamic and collisionless components in a cosmological context. At the resolution used in this work (L4), the gravitational softening is 370 pc and the typical particle/cell masses are  $3 \times 10^5$  and  $5 \times 10^4 M_{\odot}$  for the dark matter and gas, respectively. The Auriga galaxy formation model includes subgrid prescriptions for several important physical processes, such as star formation, supernova feedback, gas cooling, metal enrichment, and magnetic fields (see Grand et al. 2017 for more details). The Auriga suite was run with the *Planck* cosmology (Planck Collaboration XVI 2014) with parameters  $\Omega_M = 0.307$ ,  $\Omega_b = 0.048$ ,  $\Omega_{\Lambda} = 0.693$ , and  $H_0 = 67.77 \text{ km s}^{-1}$ .

Subhaloes in the Auriga haloes are identified using the SUBFIND algorithm, and we use the position and velocity of the main subhalo calculated by SUBFIND to define the centre of the host. The Auriga galaxies match well a number of observed properties of disc galaxies, such as their sizes, rotation curves, stellar masses, chemistry, and star formation rates (Grand et al. 2016, 2017, 2018; Marinacci et al. 2017). In addition, the suite has been used to study the stellar haloes of disc galaxies (Monachesi et al. 2016, 2019), interpret the assembly history of the MW halo (Deason et al. 2017; Fattahi et al. 2019; Belokurov et al. 2020), study the quenching of satellite galaxies (Simpson et al. 2018), and measure the total mass of the Galaxy (Callingham et al. 2019; Deason et al. 2019; Grand et al. 2019a)

## 3 THE EDGE OF MW-MASS HALOES

We identify the ‘edges’ of MW-mass haloes in the ELVIS, APOSTLE, and Auriga simulations using both the density and the radial velocity profile as a function of radius. The former is motivated by the work by Diemer & Kravtsov (2014), who used the slope of the logarithmic density profile to identify the outer edges of dark matter haloes. Here, we apply a similar formalism, but also apply this to the stars and subhaloes. We use the radial velocity profiles in a similar manner.

Throughout this work, we give radii in units of  $r_{200m}$ , defined as the radius at which the density of a halo falls to 200 times the universal matter density at  $z = 0$  ( $\rho_m = \Omega_m \rho_{\text{crit}}$ ). We also give radial velocities in units of  $v_{200m}$ , where  $v_{200m} = \sqrt{GM_{200m}/r_{200m}}$ . Diemer & Kravtsov (2014) show that  $r_{200m}$ , rather than the commonly used  $r_{200c}$ , is a more natural choice to scale haloes at large

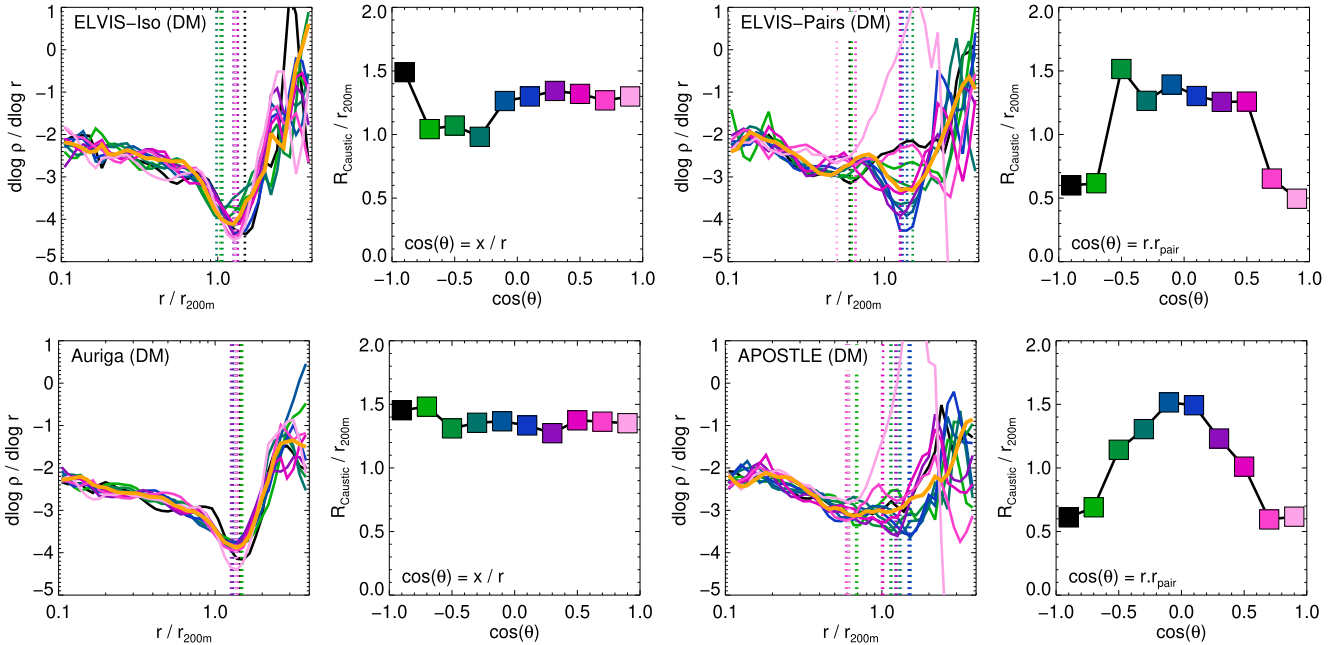


**Figure 1.** The logarithmic slope profile,  $d \log(\rho)/d \log(r)$ , of the dark matter density profiles for the ELVIS (isolated and paired), Auriga, and APOSTLE haloes. Here, 40 evenly spaced bins in  $\log(r/r_{200m}) \in [-1.0, 0.6]$ . The logarithmic profile is computed using the fourth-order Savitzky–Golay smoothing algorithm over the 15 nearest bins (Savitzky & Golay 1964). The thick orange line indicates the slope of the stacked median profile, and the coloured lines indicate the density profiles along different intervals in position angle. Ten intervals are equally spaced in  $\cos(\theta)$ . For pairs of haloes, the position angle is defined relative to the vector joining the two haloes ( $\cos(\theta) = r \cdot r_{\text{pair}}$ , so  $\cos(\theta) = 1$  is directly towards the neighbouring halo). For the isolated haloes, the position angle is arbitrary (we take  $\cos(\theta) = x/r$ ). The dotted vertical lines show the minimum, defined as  $R_{\text{Caustic}}$ , of the logarithmic slope profile in each position angle interval. The adjacent panels show  $R_{\text{Caustic}}$  as a function of the position angle. Here, the colours of the filled square symbols correspond to the coloured lines. For isolated haloes, the minima are fairly constant; however,  $R_{\text{Caustic}}$  can vary significantly for paired haloes (between  $0.6r_{200m}$  towards/away from the companion, and  $1.4r_{200m}$  perpendicular to the companion). This shows that the presence of a companion affects the outer caustic (often called the ‘splashback’ radius) of dark matter haloes.

radii. However, as we will show,  $r_{200c}$  (or even  $r_{\text{vir}}$ ; Bryan & Norman 1998; Eke et al. 1998) may be a more appropriate choice to define the edges of MW-mass haloes. Note, for a typical NFW profile with concentration,  $c = 10$ ,  $r_{200m} \approx 1.6r_{200c}$ .

### 3.1 Dark matter

We first focus on the dark matter profiles of the haloes. For the radial density profiles, we use 40 evenly spaced bins in  $\log(r/r_{200m})$  between  $-1.0$  and  $0.6$ . The logarithmic slope profile,  $d \log(\rho)/d \log(r)$ , is computed using the fourth-order Savitzky–Golay smoothing algorithm over the 15 nearest bins (Savitzky & Golay 1964). This choice of smoothing length allows us to identify the strongest features in the profile, and removes most of the noise (cf. Diemer & Kravtsov 2014). The significance of the logarithmic slope profile for dark matter haloes is discussed in detail in Diemer & Kravtsov (2014). For quiescent MW-mass haloes, the profile has a slowly steepening slope out to  $\sim r_{200m}$ , and then flattens to a slope of  $-1$  at larger radii as the halo approaches the two-halo term of the halo–mass correlation function (e.g. Hayashi & White 2008), where it is dominated by particles in different haloes. The transition between steepening and flattening results in a pronounced ‘dip’ in the logarithmic slope profile.

First, we consider stacked density profiles of each simulation suite (ELVIS, APOSTLE, and Auriga) at various position angles. We split each halo into intervals in position angle ( $0.2$  width in  $\cos(\theta)$ ) and compute the radial density profile in each interval. We then calculate the median stacked density profile in each interval for the entire halo

sample. For the paired haloes, the position angle is defined relative to the vector joining the two haloes,  $\cos(\theta) = r \cdot r_{\text{pair}}$ . Thus,  $\cos(\theta) = 1$  is directly towards the neighbouring halo. For isolated haloes, this position angle is arbitrary and we define  $\cos(\theta) = x/r$ , where the axes  $x$ ,  $y$ , and  $z$  are randomly chosen in the simulation box. In Fig. 1, we show the slopes of the median stacked profiles. The different coloured lines show 10 equally spaced intervals in  $\cos(\theta)$ , and the thick orange line shows the logarithmic slope profile of the median density profile over all position angles. For the logarithmic slope profile of the median density profile (thick orange line), we take the median density in each radial bin (over all haloes and position angles) and then compute the logarithmic slope profile. This is not the same procedure as taking the median of logarithmic slope profiles for each position angle (shown with the coloured lines), so the median profile does not always lie in the middle of these lines. The same procedure is used in subsequent plots when we show the slope profile of the median density. The dotted vertical lines indicate the most prominent minima of  $d \log(\rho)/d \log(r)$  for each position angle. Note these minima are chosen to have  $d \log(\rho)/d \log(r) < -2.5$  to minimize the effect of noise. The location of these minima,  $R_{\text{Caustic}}/r_{200m}$ , which we use to define the caustics, is shown as a function of position angle in the adjacent panels. Note that although we show stacked profiles over several haloes, the profiles in each position angle interval are subject to the effects of substructure. When averaging over all position angles, we can account for this (see below). However, here we explicitly check that removing substructures from the analysis does not significantly affect the results.

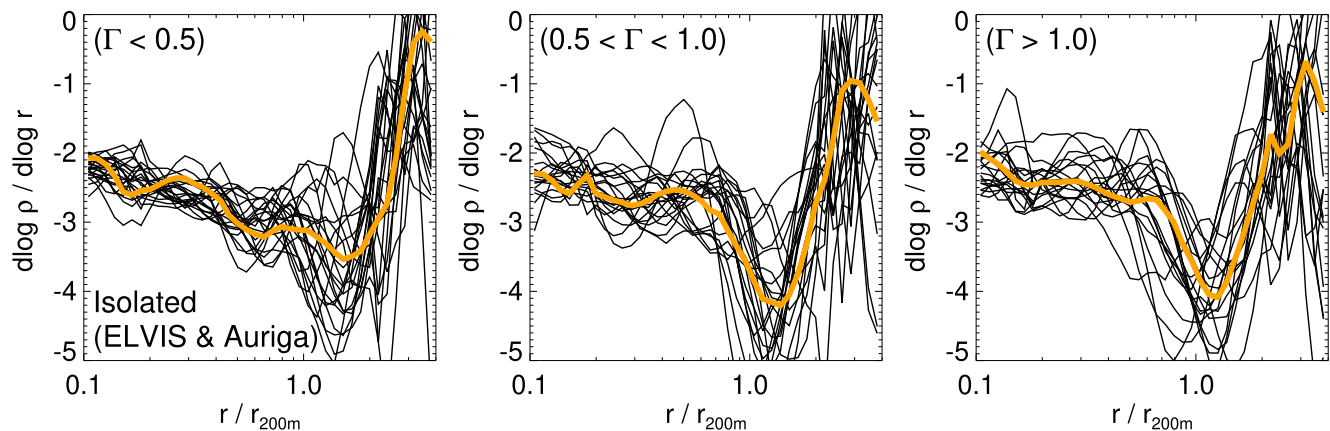


**Figure 2.** The logarithmic slope profile,  $d \log(\rho)/d \log(r)$ , of the dark matter density profiles for the isolated ELVIS and Auriga haloes. Here, we show three bins of recent mass accretion rate,  $\Gamma$ , increasing from the left- to right-hand panels. The black lines show individual halo profiles, and the thick orange line indicates the logarithmic slope of the median density profile for each mass accretion rate bin. The feature we have termed the second caustic, which is a less pronounced than the splashback radius and is located at smaller radii, becomes more evident for low-mass accretion rates.

Previous work (e.g. Adhikari et al. 2014; Diemer & Kravtsov 2014; More et al. 2015; Diemer et al. 2017) has used the location of these minima,  $R_{\text{caustic}}$ , in dark matter haloes to define the so-called ‘splashback’ radius, which is predicted in spherical models of secondary collapse (e.g. Fillmore & Goldreich 1984; Bertschinger 1985). For isolated haloes (ELVIS-Iso, Auriga), the location of this caustic shows little variation with the position angle and is typically located at  $1.4r_{200m}$ . The location of this feature is in good agreement with the location of the outermost caustic (splashback) measured in previous studies for MW-mass haloes (Diemer & Kravtsov 2014; More et al. 2015). Note that some variation with the position angle is expected as the accretion of dark matter is not isotropic (see e.g. Mansfield et al. 2017); however, as the definition of  $\cos(\theta)$  is arbitrary for isolated haloes, we do not expect to see large differences in the stacked profiles.

The location of the minimum in the paired haloes is less clear than in the isolated haloes. Here there is more variation in  $R_{\text{caustic}}$ , and the overall median stacked profile (solid orange line) appears to have two minima. The variation in the location of  $R_{\text{caustic}}$  is not random. For position angles directly towards and away from the neighbouring halo,  $R_{\text{caustic}}$  is significantly smaller ( $R_{\text{caustic}}/r_{200m} \sim 0.6$ ) than in other directions. It is unsurprising that the caustic towards the neighbour is affected: Here, the typical splashback radius ( $\sim 1.4r_{200m}$ ) runs into the neighbouring halo. However, it is less obvious why the directly opposite direction should be affected. For paired haloes, the dynamics of the particles are governed by the effective potential of the two massive haloes, and there is a ‘saddle point’ in the potential at  $\cos(\theta) = 1$ . Our interpretation is that along this direction particles can only accrete from a limited distance due to the presence of the neighbour. This material will then have less time to accelerate before it reaches apocentre due to its smaller starting distance, and thus will reach a smaller apocentre on the opposite side (i.e. at  $\cos(\theta) = -1$ ). Another possibility is that distribution of mass in the  $\cos(\theta) = -1$  direction is due to the Lagrange points of the effective potential that are expected in that direction. In this scenario, particles that go beyond the Lagrange points of the effective potential escape, and at  $\cos(\theta) = -1$ , we are seeing a feature shaped by the presence of a such a Lagrange point, which is closer than it would be for an isolated halo.

The location of a second caustic at smaller radii has been seen in previous work (see e.g. figs 10, 13, and 14 in Diemer & Kravtsov

2014) and has been demonstrated explicitly in (Adhikari et al. 2014, see their fig. 9). Adhikari et al. (2014) show that for slowly accreting haloes, the stream of splashback material is separated from the rest of the virialized matter in the halo, and the location of the second caustic becomes more pronounced. The majority of MW-mass haloes are slowly accreting (especially relative to cluster-sized haloes), so it is particularly intriguing that we detect this feature here. Curiously, the typical location of this second caustic corresponds to  $r_{200c}$ , rather than  $r_{200m}$  (as  $r_{200m} \sim 1.6 \times r_{200c}$ ). We first noted this secondary feature in the paired haloes; however, this feature is also apparent in the individual profiles of the isolated haloes. This feature can be difficult to see in the stacked profiles in Fig. 1 as there is considerable halo-to-halo scatter, and the signal is relatively weak (especially relative to the splashback radius for isolated haloes). In Fig. 2, we show the logarithmic slope profiles for individual haloes in the isolated ELVIS and Auriga runs. Here, we separate the haloes into three bins with increasing (recent) mass accretion rate from the left to right-hand panels. The thick orange lines show the logarithmic slope profile of the median density profiles in each bin (where the differential profile is computed after finding the median density in each radial bin, as described above). We use the definition given by Diemer & Kravtsov (2014) to define the mass accretion rate:

$$\Gamma = \frac{\log M_{\text{vir}}(z_1) - \log M_{\text{vir}}(z_2)}{\log(a_1) - \log(a_2)}, \quad (1)$$

where  $z_1 = 0$  and  $z_2 = 0.5$ . Note when computing the individual halo profiles we compute the median value over 10 equally spaced intervals in position angle (i.e. 0.2 width in  $\cos(\theta)$ ) for each radial bin. This procedure has the advantage of minimizing the effect of substructure in the profile (Mansfield et al. 2017). We have checked that explicitly removing (bound) substructures produces very similar results; however, we do caution that there are other inhomogeneities present in the density that could effect the results, but we expect that our procedure will account for the most prominent irregularities. Fig. 2 illustrates two important points. First, as mentioned above, there is wide range in halo-to-halo scatter, particularly, for any second caustic features. Secondly, the second caustic becomes more prominent at lower mass accretion rates, as predicted by Adhikari et al. (2014). Note that the stacked profiles, particularly at low accretion rates, hint at three separate caustics

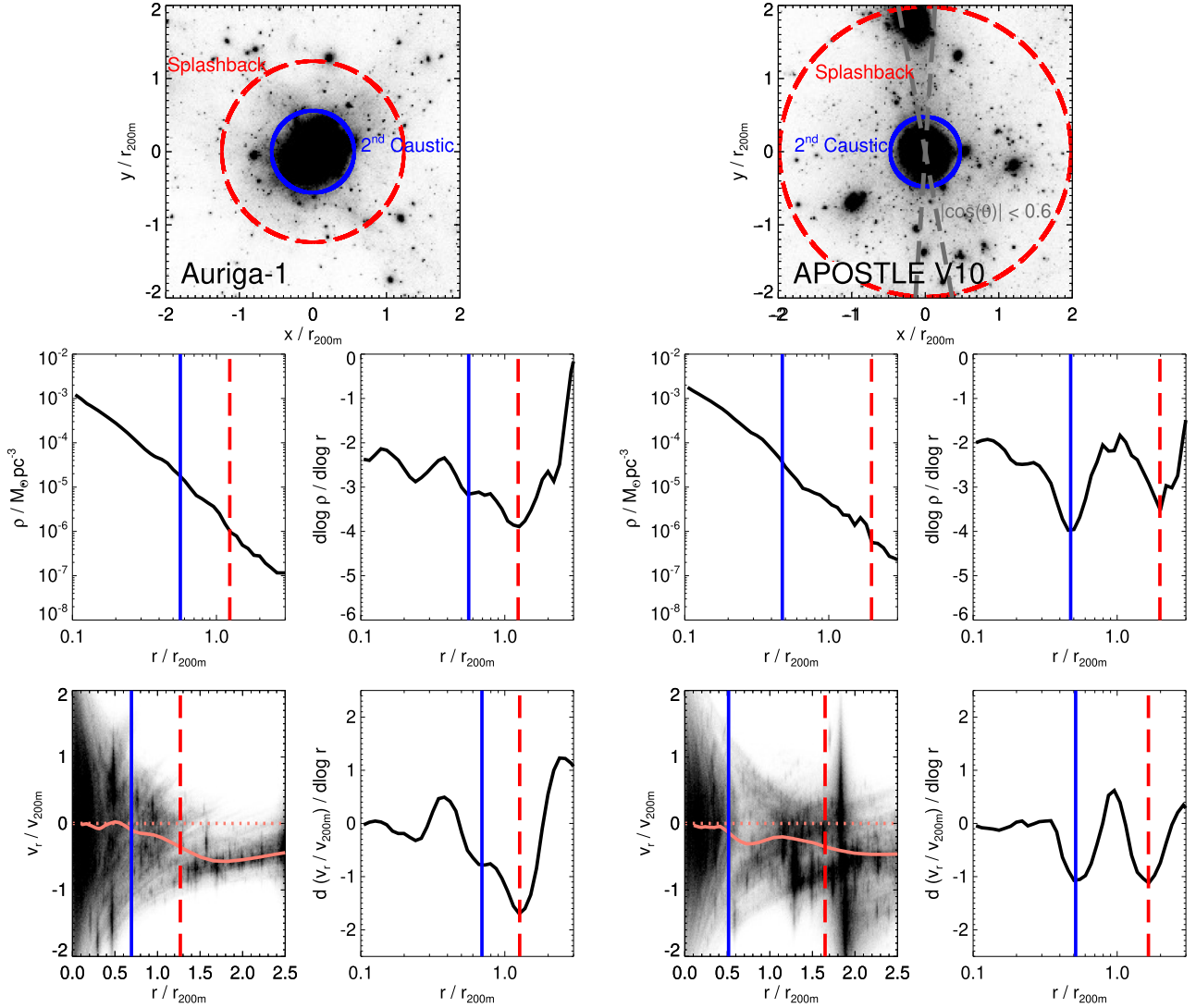


**Figure 3.** Two example haloes from Auriga (left-hand panels) and APOSTLE (right-hand panels). Here we show the density of dark matter in  $(x, y)$  projection (top panels), the radial density profiles (middle panels), and the radial velocity profiles (bottom panels). The shading in the top and bottom (left-hand) panels shows  $200 \times 200$  pixels saturated at the 95th percentile of the 2D histogram. In addition to the density and radial velocity profiles, we also show the logarithmic slope profiles of these quantities:  $d \log(\rho)/d \log(r)$  and  $d(v_r)/d \log(r)$ . These logarithmic slope profiles are used to identify caustics in the dark matter. The vertical lines indicate the splashback radius (red dashed lines) and the second caustic (blue solid line). These radii, computed from the density profile, are also shown in the top panels. The position angles excluded in the paired haloes to compute these quantities are shown in the top right-hand panel ( $|\cos(\theta)| < 0.6$ ). The radial velocity profiles (the solid pink lines show the median profile, and the dotted pink line indicates the zero level for reference) suggest that the splashback radius is related to the material infalling on to the haloes for the first time, and the second caustic relates to the edge of the virialized material, which has undergone at least two orbital passages through pericentre. The caustics defined in density or velocity space are closely related, albeit with some scatter (see Fig. 4).

in the logarithmic density profile. The very inner ‘dips’ likely correspond to the apocentres of early, massive mergers in the halo’s assembly history. However, we caution against overinterpretation of these features as they can have low significance. Finally, it is worth noting that, although we see evidence for a second caustic in both paired and isolated haloes, it is not necessary true that the origin of the caustic is the same in both cases. Indeed, there could be multiple, interconnected causes for this interesting feature in Galactic-sized haloes. We now explore the second caustic feature further by analysing individual haloes in more detail.

In Fig. 3, we show two example haloes. The left-hand panels show the dark matter distribution of Auriga-1 (an isolated halo), and the right-hand panels show APOSTLE V10 (a paired halo:

in Fig. 3, the coordinate system is centred at  $(x, y, z) = (61.948, 24.230, 48.305)$  Mpc in the V10 system; see table A1 in Fattahi et al. 2016). The top panels show a 2D projection of the dark matter distribution, the middle panels show the density profile and logarithmic slope profile, and the bottom panels show the radial velocity profile and corresponding logarithmic slope profile. The dashed red lines indicate the splashback radius and the solid blue line indicates the second caustic. For the paired haloes, caustics are identified by excluding position angles with  $|\cos(\theta)| > 0.6$ . The second caustic is located at a smaller radius and is less pronounced than the splashback radius. We generally find that the second caustics are easier to identify in the individual halo density profiles than in the stacked profiles (see e.g. Figs 1 and 2). This is likely

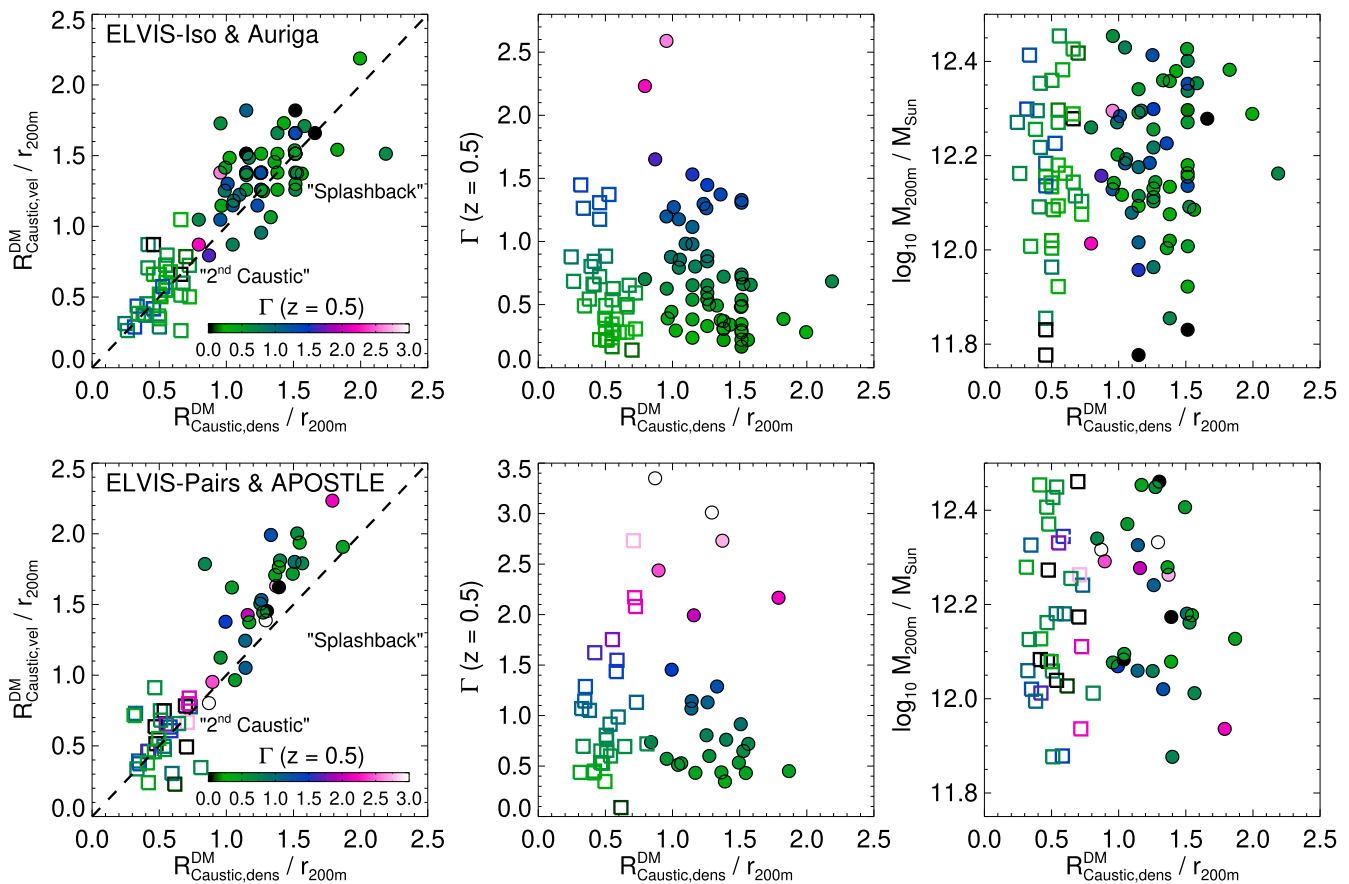


**Figure 4.** The dark matter caustics of individual haloes in isolated (top panels) and paired (bottom panels) environments. The left-hand panels show the position of the density caustics against the radial velocity caustics. The filled circles indicate the splashback radius and the open squares indicate the second caustics. The dashed lines show the one-to-one relation. The splashback radii are more poorly defined in the paired haloes (e.g. in  $\sim 20$  per cent of the paired haloes a splashback radius cannot be clearly identified). However, the properties of the second caustics are similar between paired and isolated haloes. The symbols are coloured according to the mass accretion rate,  $\Gamma(z = 0.5)$ . For haloes with rapid recent accretion, the splashback radius tends to be smaller, and closer to the second caustic. Indeed, most cases in which *two* caustics could not be clearly identified have relatively high  $\Gamma$ . The middle panels show the mass accretion rate against the radius of the dark matter caustics, and the right-hand panels show the  $(z = 0)$  halo masses against the dark matter caustics.

because the feature is relatively weak and gets smeared out over a range of radii when the profiles are stacked together.

The second caustic can also be seen in the radial velocity profile. Here, we use the local minimum of  $d(v_r)/d\log(r)$  to identify the caustics. The velocity and density caustics typically align on average, but there is some scatter (see Fig. 4). The radial velocity profile allows us to see more clearly what the second caustic is. The feature looks similar to the second caustic features shown in Adhikari et al. (2014), and we suggest that this feature relates to the edge of the material in the halo at the position where particles have completed at least two passages through pericentre. The splashback radius is located where material is outgoing for the first time, and particles have only completed one pericentric passage. The existence of two caustics, each defining different regions of the halo, begs the question: Which should we use to define the edge of the halo? This question is particularly relevant for low-mass accreting haloes, where the splashback and second caustic are well separated (Adhikari et al. 2014). Our MW is located in the LG and neighbours a massive halo, so the definition of splashback radius is less clear (and indeed overlaps with the halo of M31). For this reason, we suggest that the most meaningful radius for the MW is the second caustic. We will show in Section 3.2 that this definition is

also applicable to the stellar material. Note, however, that although we have defined this interesting feature as the ‘second caustic’, this does not necessarily correspond to the classical definition of second caustic from spherical (or ellipsoidal) collapse models (as seen in Adhikari et al. 2014). In particular, the wide halo-to-halo scatter, and the apparent correlation with the stellar distribution (see following section), could point to a merger origin, i.e. from the apocentre of the last major merger. In addition, we caution that the second caustic, as we have defined it in this work, could have multiple origins that vary from halo to halo. The actual origin of this feature will require further investigation, ideally with particle evolution tracking.

In Fig. 4, we show the positions of the dark matter caustics for individual haloes in isolated (top panels) and paired (bottom panels) environments. The caustics are identified as minima in the  $d\log(\rho)/d\log(r)$  and  $d(v_r)/d\log(r)$  profiles. We consider the two most prominent (outer) caustics, and only consider features with  $d\log(\rho)/d\log(r) < -2.5$  and  $d(v_r)/d\log(r) < -0.25$ , respectively. In addition, for every individual halo, we visually inspect the profiles to ensure we are not confusing noise with a real caustic. The left-hand panels show the position of the velocity caustics against the density caustics. The filled circles show the splashback radii and the open squares show the second caustics. Note that for isolated

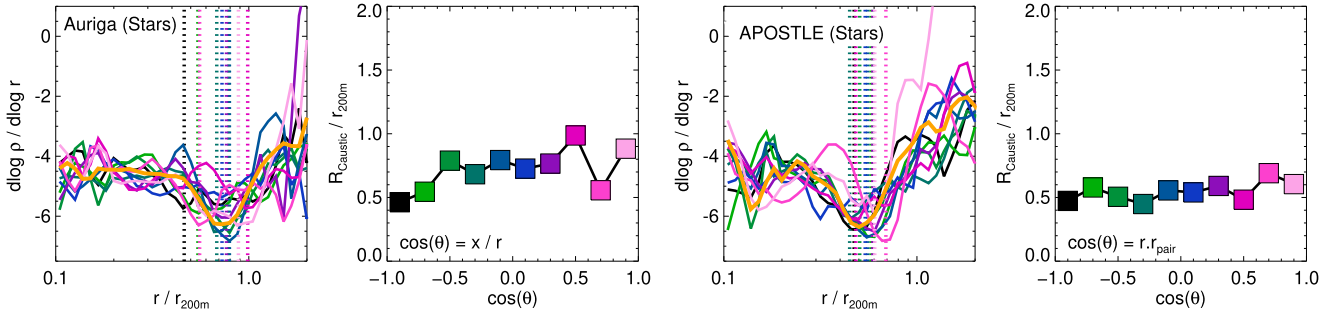


**Figure 5.** The logarithmic slope profile,  $d \log(\rho)/d \log(r)$ , of the stellar density profiles of the Auriga (left-hand panels) and APOSTLE (right-hand panels) haloes. Here, 40 evenly spaced bins in  $\log(r/r_{200m})$  have been used in the range  $\log(r/r_{200m}) = [-1.0, 0.6]$ . The logarithmic profile is computed using the fourth-order Savitzky–Golay smoothing algorithm over the 15 nearest bins (Savitzky & Golay 1964). The thick orange line indicates the logarithmic slope profile of the median density profile, and the coloured lines show the slope profiles along different intervals in the position angle. Ten intervals are equally spaced in  $\cos(\theta)$ . For pairs of haloes, the position angle is defined relative to the vector joining the two haloes ( $\cos(\theta) = r \cdot r_{\text{pair}}$ , so  $\cos(\theta) = 1$  is directly towards the neighbouring halo). For the isolated haloes, the position angle is arbitrary (we take  $\cos(\theta) = x/r$ ). The dotted vertical lines show the minimum, defined as  $R_{\text{Caustic}}$ , of the logarithmic slope profile in each position angle interval. The adjacent panels show  $R_{\text{Caustic}}$  as a function of position angle. The colours of the filled squares correspond to the coloured lines. The caustics for paired and isolated haloes are similar, and are typically located at  $0.6r_{200m}$ .

haloes, the splashback radius can be identified in almost all of the haloes; however, even with a restriction on the position angle, this can be harder to detect in the paired haloes. Over all paired haloes (in ELVIS and APOSTLE), 21 per cent have no detectable splashback radius in density or velocity. Moreover, the density and velocity caustics are not as closely aligned in the paired environments. On the other hand, the detection efficiency of the second caustic is very similar between isolated and paired haloes of similar mass (e.g. by comparing ELVIS Isolated and Paired haloes). There is no discernible second caustic in 16 per cent of the haloes (over all haloes in ELVIS, APOSTLE, and Auriga), and the non-detections are typically more massive haloes with higher recent accretion rates (see Fig. 2). The detected second caustics range in radii between  $0.3$  and  $0.8r_{200m}$  and have density slopes at these radii of  $\sim -2.5$  to  $-4.5$ .

The symbols in Fig. 4 are coloured according to the recent mass accretion rate (see equation 1). The majority of haloes have quite low recent mass accretion rates ( $\Gamma < 1$ ), as expected for MW-mass haloes. The middle panels of Fig. 4 show how the positions of the caustics relate to  $\Gamma$ . The caustics in the isolated haloes are typically at smaller radii for haloes with higher recent mass accretion rates (as shown in Diemer et al. 2017 over a wider mass range). However, this trend is not present in the paired environments, particularly for  $\Gamma > 1.5$ . This is likely because the splashback radius and the second caustic run into each other at higher mass accretion rates, and are harder to distinguish. Furthermore,  $\Gamma$  is poorly defined in paired environments where the outer profiles of the neighbouring haloes overlap. Finally, we show the location of the caustics as a function of halo mass in the right-hand panels. We see very little dependence between  $R_{\text{Caustic}}/r_{200m}$  and halo mass. Indeed, analytical models predict that the mass accretion rate, rather than halo mass, is the more important physical quantity that determines the splashback radius (e.g. Adhikari et al. 2014).

### 3.2 Stars

We now turn our attention to the stellar material in MW-sized haloes. We analyse the APOSTLE and Auriga simulations that include baryonic material. In Fig. 5, we show the logarithmic slope of the stellar density profiles of the Auriga (left-hand panels) and APOSTLE (right-hand panels) haloes. We use the same bin sizes and smoothing technique as for the dark matter. As in Fig. 1, the

median stacked profiles are shown, and the different colours show 10 different intervals in the position angle. The solid orange line shows the logarithmic slope of the median density profile for all haloes over all position angles. We indicate the minimum in the logarithmic slope for each position angle with dotted lines and we only consider minima with  $d \log(\rho)/d \log(r) < -5$  (although, typically, the stellar caustics are much stronger than this, and are in the range  $-15 < d \log(\rho)/d \log(r) < -5$ ). The location of these minima are shown as a function of position angle in the adjacent plots (and colour coded accordingly). There is some variation of  $R_{\text{Caustic}}$  with the position angle, but there is no obvious trend. It is notable that the profiles of the paired haloes (APOSTLE) and isolated haloes (Auriga) are similar, and the caustics are typically found at  $0.6r_{200m}$ . Interestingly, this is exactly the radius that we identified in Fig. 1 as the second caustic in the dark matter. Below, we focus on the profiles of individual haloes, and explicitly examine this apparent connection between the stars and dark matter.

We also show the logarithmic slope of the *projected* stellar density profiles in Fig. 6. Here we show the stacked profiles of all Auriga (left-hand panels) and APOSTLE (right-hand panels) haloes. This 2D measure is relevant for stellar halo density profiles of external MW-mass galaxies for which only two spatial coordinates are known. The three different linestyles indicate three (random) projections, and the dotted red line shows the stacked 3D profile (repeated from Fig. 5 for comparison). A well-defined ‘edge’ is also seen in the projected profiles. This occurs at slightly lower radii (in projection) relative to the 3D radius (by  $\sim 0.1r_{200m}$ ), and is a weaker feature than in the 3D profiles. However, the clear detection in 2D is encouraging for studies of external stellar haloes. Currently, surveys like Ghosts (Harmsen et al. 2017) and Dragonfly (Merritt et al. 2016) are only able to probe the stellar halo density out to  $\sim 50$ – $80$  kpc. However, with deeper observations and future wide-field facilities such as the Nancy Grace Roman Space Telescope (Spergel et al. 2015), the radial range of interest, beyond 150 kpc should be accessible for nearby galaxies. Furthermore, the signal of the stellar edge could be enhanced by stacking the profiles of several galaxies.

In Fig. 7, we show the stellar distribution of two example haloes, Auriga-1 on the left-hand panels and APOSTLE V10 on the right-hand panels. The top panels show a 2D projection, the middle panels show the stellar density and logarithmic slope profiles, and the



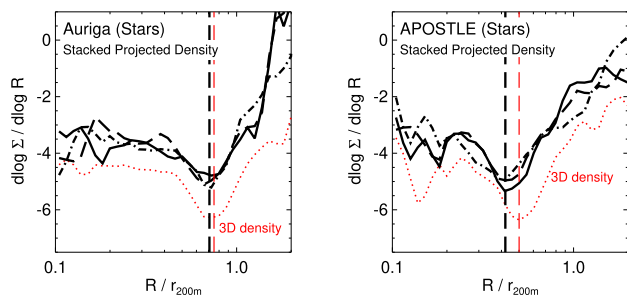


**Figure 6.** The logarithmic slope profile,  $d \log(\Sigma)/d \log(R)$ , of the stellar surface density profiles of the Auriga (left-hand panels) and APOSTLE (right-hand panels) haloes. Here, 40 evenly spaced bins in  $\log(R/r_{200m})$  have been used in the range  $\log(R/r_{200m}) = [-1.0, 0.6]$ . The logarithmic profile is computed using the fourth-order Savitzky–Golay smoothing algorithm over the 15 nearest bins (Savitzky & Golay 1964). The three linestyles show the stacked profiles for three (random) projections. For comparison, the logarithmic slope profile of the 3D stellar density is shown with the dotted red line (see Fig. 5). A well-defined edge is also seen in the (stacked) projected stellar density profiles, although this is a weaker feature than in the 3D case.

bottom panels show the radial velocity and associated logarithmic slope profiles. The solid orange line indicates the caustic in the stellar distribution. We typically identify only one clear outer caustic (cf. the dark matter where we commonly find two) at  $\sim 0.6r_{200m}$ . However, there can be less prominent caustics at smaller radii, which are associated with apocentres of past accretion events (these can be seen in both dark matter and stars; see e.g. Figs 3 and 7). Such a feature has already been seen in the MW halo at  $r \sim 20$  kpc, and is likely related to the apocentre of the *Gaia*-Sausage/Enceladus event (Deason et al. 2013, 2018). In this work, we are interested in the caustic that defines the edge of the stellar material, and is hence associated with the furthest apocentre of stars bound to the Galaxy. The radial velocity profiles suggests that the location of this stellar caustic coincides with the edge of the material that has completed at least two pericentric passages, similarly to the second caustic in the dark matter (see below). We find no obvious difference between the isolated and paired haloes, which is unsurprising as the location of the stellar caustic ( $0.6r_{200m} \sim r_{200c} \sim 220$  kpc) does not generally overlap with the neighbouring halo.

In Fig. 8, we examine the stellar caustics of individual haloes in more detail. We are able to identify a stellar caustic in over 90 per cent of the haloes. Those cases where we cannot clearly identify a feature (in either density or velocity) are typically cases where there is very recent accretion and the outer density profiles are messy. Note we typically only consider stellar caustics with  $d \log(\rho)/d \log(r) < -5$  or  $d(v_r)/d \log(r) < -1.0$ , which we choose to be distinct from the noise level. The left-hand panel of Fig. 8 relates the positions of the velocity and density caustics of the stars. These caustics generally coincide but there is significant scatter. The points are colour coded according to the recent (total) mass accretion rate,  $\Gamma(z = 0.5)$  (see equation 1). In the middle (density) and right-hand (velocity) panels, we relate the stellar caustics to the dark matter caustics. Solid filled symbols are used for the splashback radii of the dark matter and open squares are used for the second caustic of the dark matter. As mentioned earlier, the stellar caustics are strongly related to the second caustic in the dark matter. Note the dashed line indicates the one-to-one relation; this is not a fit! This relation holds for  $\sim (0.3-0.8)r_{200m}$ , but seems to break down at larger radii. This discrepancy at large radii is likely for two

reasons. First, when  $R_{\text{caustic}}^{\text{STAR}}$  is large, the stellar caustic can be closer to the splashback radii, or even somewhere between the second caustic and the splashback radius. Secondly, the stellar caustic is harder to define at very large distances ( $0.8r_{200m} \sim 300$  kpc) where the density of stars is very low.

We leave a more thorough analysis of how the dynamics of the star particles relate to the dark matter to future work. However, it is worth discussing the possible origin of the correlation between the caustic in the stellar material and the second caustic in the dark matter. First, we must consider that the stars and dark matter do not undergo the same evolution in the build up of a halo. A significant amount of the dark matter is assembled by ‘smooth’ accretion (e.g. Angulo & White 2010; Genel et al. 2010; Wang et al. 2011). On the other hand, the stars are assembled from a ‘lumpier’ accretion process, as the stars do not populate subhaloes below a certain mass threshold (e.g. Sawala et al. 2015). Secondly, the stripping of stars from bound subhaloes proceeds differently from the stripping of the dark matter (e.g. Peñarrubia, Navarro & McCannachie 2008; Fattahi et al. 2018): The (less bound) dark matter is stripped first, and the more centrally concentrated stars are almost always stripped close to pericentre, when almost all of the dark matter has already been peeled away.

We speculate that to lose stars to tidal forces subhaloes must typically pass through at least two pericentres, and thus the ‘edge’ of the stellar material coincides with the second caustic in the dark matter. This may be especially true in relatively major mergers, which typically dominate the mass budget of the accreted stellar halo (see e.g. Purcell, Bullock & Zentner 2007; Cooper et al. 2010; Deason, Mao & Wechsler 2016; D’Souza & Bell 2018), when such passages lead to a loss of angular momentum and shrinking of the pericentre. Finally, we remark that the relation between the ‘edges’ of stars and dark matter may vary at different mass scales. Here, we have focused on MW-mass haloes, but the non-linear stellar mass to dark matter mass relation (Behroozi, Conroy & Wechsler 2010; Moster et al. 2010; Read et al. 2017), and the varying smooth to lumpy mass accretion rate (Genel et al. 2010), will likely lead to different relations at higher and lower masses.

In Section 3.1, we discussed how the second caustic of the dark matter, which we now see coincides with the stellar caustic, may be the most relevant definition of the edge of the MW. This means that the edge of our own Galaxy is, potentially, observable in the stellar distribution. Currently, the density profile of the stellar halo has only been mapped out to  $\sim 50-100$  kpc (e.g. Deason, Belokurov & Evans 2011; Sesar, Jurić & Ivezić 2011; Deason, Wetzel & Garrison-Kimmel 2014a; Xue et al. 2015; Slater et al. 2016; Hernitschek et al. 2018). Moreover, radial velocities of stars are only available, in any significant numbers, out to similar distances (e.g. Maun et al. 2004; Deason et al. 2012; Bochanski et al. 2014; Cohen et al. 2017). However, with upcoming wide-field photometric and spectroscopic facilities like the Rubin Observatory Legacy Survey of Space and Time (LSST; Ivezić et al. 2019), the Roman Space Telescope (Spergel et al. 2015), the Mauna Kea Spectroscopic Explorer (MSE; Bauman et al. 2016), and the Subaru Prime Focus Spectrograph (PFS, Takada et al. 2014) on the horizon, exploring these extreme distances will be feasible in the near future.

Finally, it is worth discussing how the concept of galaxy edge is relevant to studies that require a definition of where the halo ends. For example, when using the escape velocity of local halo stars to estimate the total mass of the Galaxy, the definition of the radius of ‘escape’ is an important element of the analysis. Indeed, Deason et al. (2019) used a radius of  $2r_{200c}$  ( $\sim 1.25r_{200m}$ ), which is at the extreme end for the Auriga haloes. However, while this approach

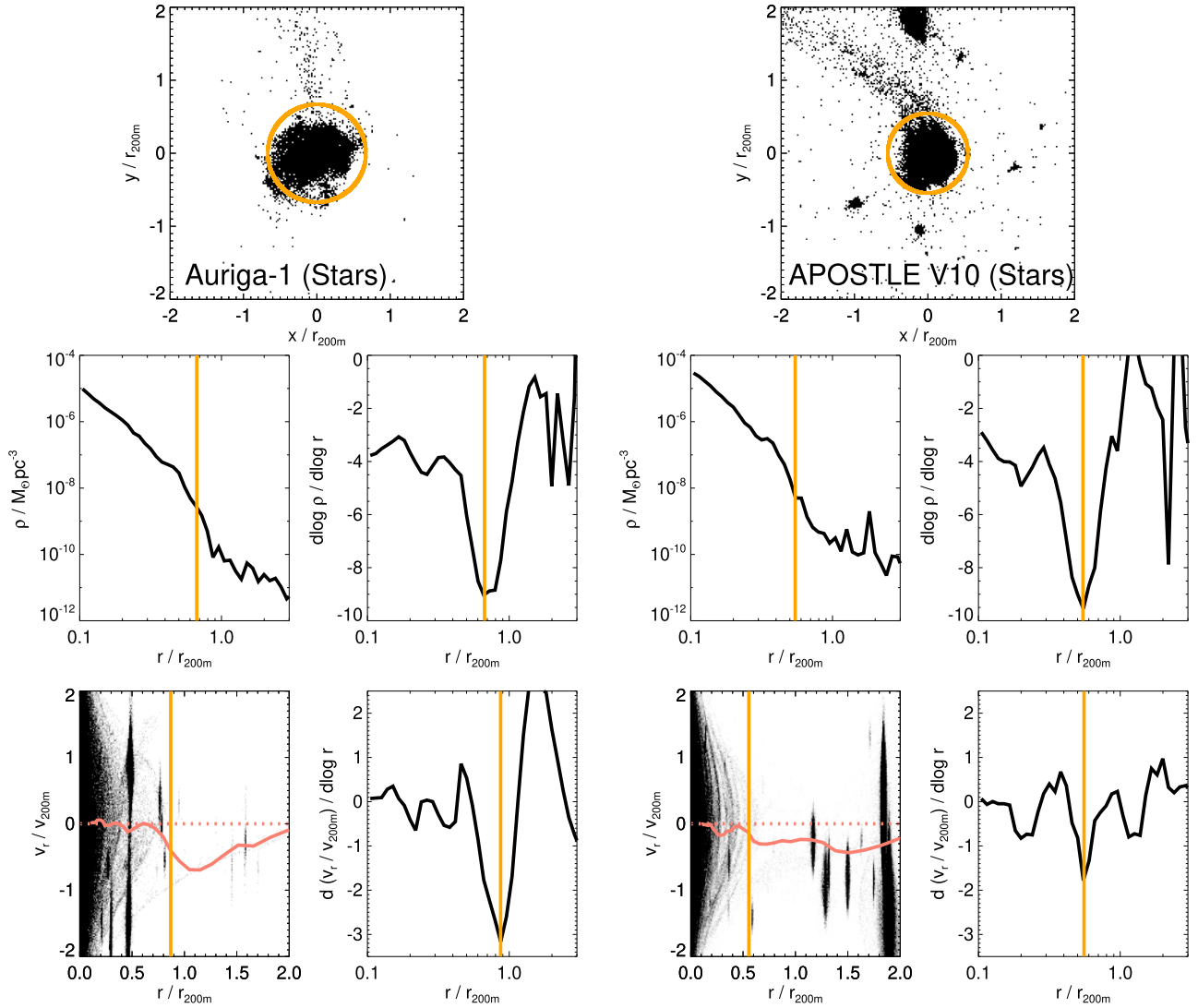


**Figure 7.** Two example haloes from Auriga (left-hand panels) and APOSTLE (right-hand panels). These are the same haloes shown in Fig. 3. Here, we show the density of stars in the  $(x, y)$  projection (top panels), the radial density profiles (middle panels), and the radial velocity profiles (bottom panels). The shading in the top and bottom (left-hand) panels shows  $200 \times 200$  pixels saturated at the 90th percentile of the 2D histogram. In addition to the density and radial velocity profiles, we also show the logarithmic slope profiles of these quantities:  $d \log(\rho)/d \log(r)$  and  $d(v_r)/d \log(r)$ . The stellar caustics are identified as minima in the logarithmic slope profiles, and are indicated with the vertical solid lines.

is conservative in that it does not allow for radii where stars can potentially escape, our results suggest that a smaller radius is likely more applicable. For example, the median stellar caustic radius of the Auriga simulations is  $0.7r_{200m}$ , which is approximately  $1.2r_{200c}$ . If this distance is used in the Deason et al. (2019) analysis to define the radius beyond which stars have escaped, then the total mass of the MW is revised upwards by 20 per cent. Interestingly, this is approximately the change that Grand et al. (2019a) found was required to correct the mass estimates when the procedure is applied to the Auriga haloes. In particular, Grand et al. (2019a) suggest that the mass estimates are underestimated because the local stars do not reach out to  $2r_{200c}$ . Here, we show that this is indeed the case. However, as a cautionary note, we should use the observed  $R_{\text{Caustic}}^{\text{STAR}}$  rather than the median value of the Auriga haloes, which does not necessarily coincide with the true MW value (see the end of Section 3.3). Finally, we note that the term ‘escape velocity’ is a misleading term when discussing the highest velocity halo stars. In

reality, much faster stars would not ‘escape’ as such, but rather they just do not exist in the stellar distribution.

### 3.3 Subhaloes and dwarf galaxies

In the previous subsections, we have focused on the distribution of dark matter and stars. Now we apply a similar analysis to the subhalo population. In this case, the number of discrete tracers is much lower than for the dark matter or star particles. For this reason, we concentrate only on the caustics defined in velocity space, where it is easier to identify features associated with caustics when there are low numbers of tracers. It is worth noting that there is no division into position angle sectors here (cf. the dark matter and stars), which makes the subhalo-based profiles sensitive to substructure. Thus, although this analysis is a valuable first step, we plan to apply more sophisticated techniques tailored towards highly discretely sampled distributions in future work.

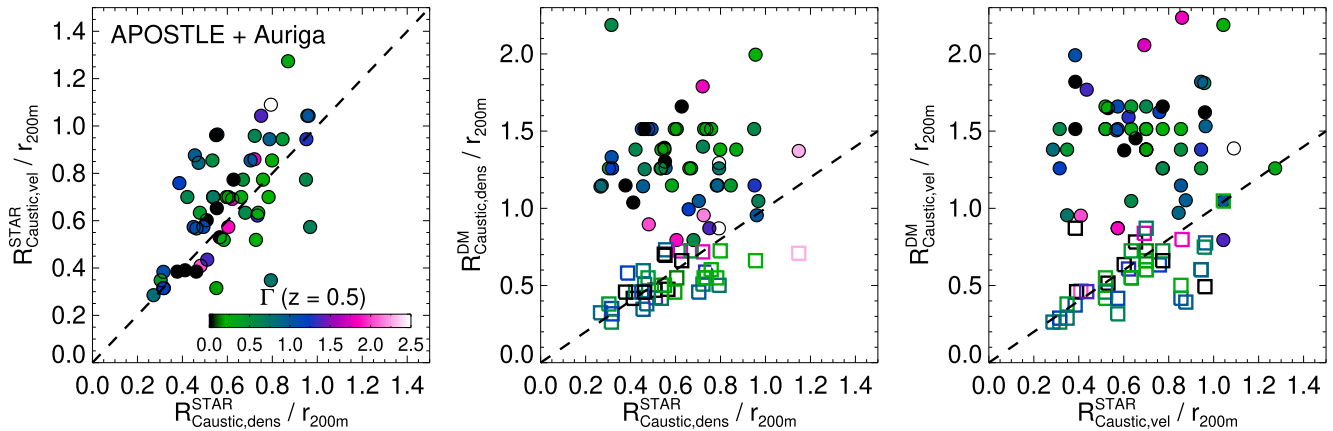


**Figure 8.** The positions of the stellar caustics in Auriga and APOSTLE haloes. The left-hand panel shows the radii of the stellar density caustics against the radii of the stellar radial velocity caustics. The middle and right-hand panels show the radii of the stellar density (middle panel) and velocity (right-hand panel) caustics against those of the dark matter caustics. The filled circles and open squares indicate the dark matter splashback and second caustic radii. The symbols are coloured according to the mass accretion rate,  $\Gamma(z = 0.5)$ . The dashed lines show the one-to-one relation. Note that the DM caustics at large radii appear discretized owing to the logarithmic binning. Over a wide range in radii (out to  $\sim 0.8r_{200m}$ ), the stellar caustics correspond to the second caustic in the dark matter. In a few cases where  $R_{\text{Caustic}}^{\text{STAR}}$  is large, the stellar caustic can lie in between the dark matter caustics, and can even be closer to the splashback radius.

We use the (dark-matter-only) ELVIS suite to study the general subhalo population, and APOSTLE and Auriga to analyse the ‘dwarf’ population. Here we do not distinguish between isolated and paired environments and, in the paired cases, only consider subhaloes with  $|\cos(\theta)| < 0.6$  to identify caustics. We define subhaloes as all bound substructures with  $M_{\text{Sub}}^{\text{DM}} > 10^{7.3} M_{\odot}$ . This is the convergence limit for subhaloes found by Garrison-Kimmel et al. (2014). In APOSTLE and Auriga, subhaloes with at least one star particle are identified as luminous dwarfs. This approximately corresponds to subhaloes with  $M_{\text{Sub}}^{\text{Star}} > 10^5 M_{\odot}$ .

For each individual halo, we use the logarithmic slope of the radial velocity profile to define the caustics in the subhalo population. Note that for the dwarf galaxies, where the numbers of objects are typically low ( $O(100)$  per halo), we change the binning in logarithmic radius to have 25 equally spaced bins in the range  $\log(r/r_{200m}) \in [-1.0, 0.5]$  and use the same smoothing kernel as in the previous subsections. Due to the small numbers, we only identify the most prominent caustic and do not attempt to find two distinct caustics.

The resulting caustics are shown in Fig. 9 as a function of the (two) dark matter caustics (computed in Section 3.1). Caustics can be identified for the majority of subhalo populations, but in several cases (30 per cent), a caustic could not be identified in the dwarf population, mainly as a result of small numbers. The filled grey circles in Fig. 9 indicate the splashback radii in the dark matter and the filled red squares indicate the second caustic in the dark matter. Interestingly, we find that the caustic in the subhalo population corresponds to the splashback radius (left-hand panel), while the caustic in the luminous dwarfs’ population coincides with the second caustic in the dark matter (right-hand panel). This is perhaps unsurprising as the subhalo population traces the dark matter, while the luminous dwarfs are more closely related to the accretion of the more massive subhaloes, and hence the stellar halo.

We show two examples for the dwarf galaxy population in Auriga-16 (top panel) and APOSTLE-V5 (bottom panel; centred on  $(x, y, z) = (42.867, 88.474, 93.675)$  Mpc) in Fig. 10. The caustics are not as clearly defined as in the dark matter or stars, but, importantly, there are already observations of luminous dwarf tracers out to large

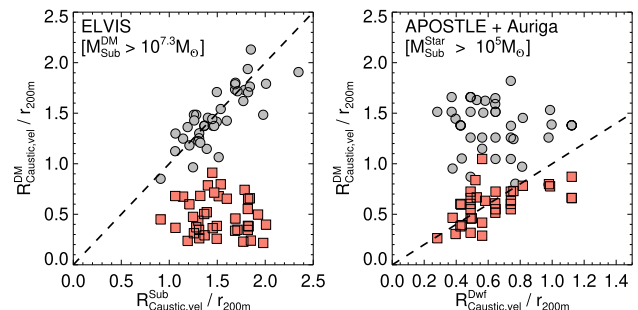


**Figure 9.** The radius of the dark matter caustics against that of subhalo/dwarf caustics. We focus only on the velocity caustics that are more easily identified with low numbers of tracers. In the left-hand panel, we show all subhaloes in ELVIS down to the resolution limit. Dwarfs, defined as subhaloes with at least one star particle, in the Auriga and APOSTLE simulations are shown in the right-hand panel. We only aim to identify one caustic for the subhalo populations, owing to low-number statistics. Thus, the two types of symbols shown in these plots relate to the two caustics in the dark matter (splashback = filled grey circles, second caustic = filled red squares). For the subhaloes in ELVIS (left-hand panel), this generally corresponds to the splashback radius (filled grey circles) of the dark matter particles. However, the caustic defined by the luminous dwarfs in APOSTLE and Auriga (right-hand panel) corresponds to the second caustic (filled red squares) in the dark matter. Note in several cases ( $\sim 30$  per cent) a caustic could not be identified in the luminous dwarfs, most commonly due to low numbers.

distances in the LG, so this analysis is observationally motivated. In Fig. 11, we perform the same analysis on the *observed* dwarfs. Here, we use the latest compilation of dwarfs from McConnachie (2012), and show physical radius and velocity (rather than in units of  $r_{200m}$  and  $v_{200m}$ ). The distances and radial velocities are converted to Galactocentric coordinates, assuming a circular velocity of  $v_c(r_0) = 235 \text{ km s}^{-1}$  at the position of the Sun ( $r_0 = 8.1 \text{ kpc}$ ), and a peculiar solar motion of  $(U_{\odot}, V_{\odot}, W_{\odot}) = (11.1, 12.24, 7.25) \text{ km s}^{-1}$  (Schönrich, Binney & Dehnen 2010). We use 22 radial bins equally spaced in  $\log(r)$  between 1.0 and 3.3. As

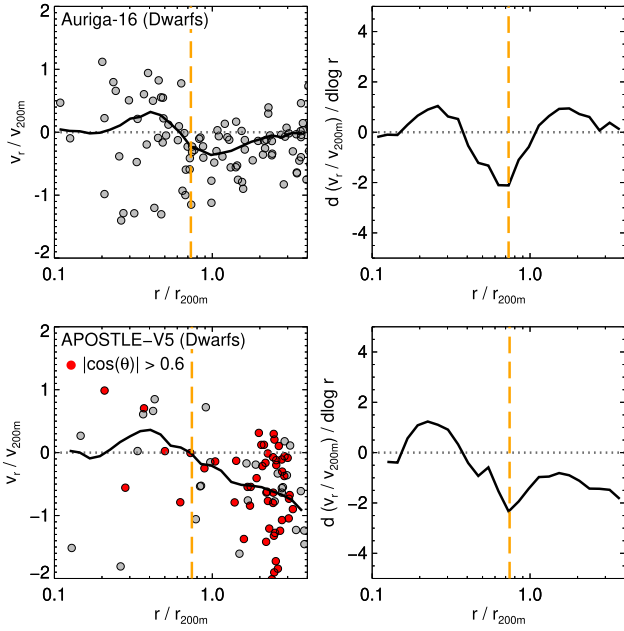


**Figure 10.** Examples of caustics defined from the luminous dwarf population in Auriga (Au-16, top panels) and APOSTLE (V5, bottom panels). The left-hand panels show the radial velocities of the dwarfs as a function of radius. The paired halo dwarfs with  $|\cos(\theta)| > 0.6$  (i.e. close in angle to the line joining the two haloes) are indicated in red. The right-hand panels show the logarithmic slope profiles of the radial velocities. The vertical dashed line indicates the caustic.

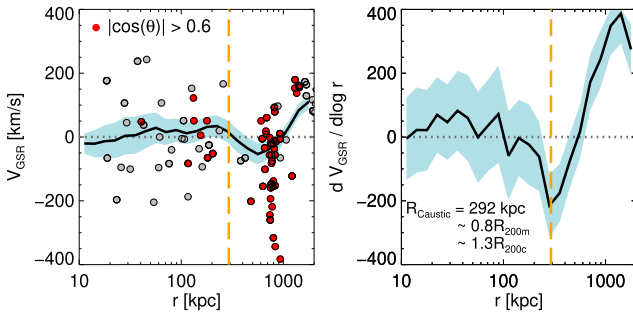


**Figure 11.** Left-hand panel: the radial velocities (in Galactocentric coordinates,  $V_{\text{GSR}}$ ) of observed LG dwarf galaxies. Dwarfs with  $|\cos(\theta)| > 0.6$  (i.e. close in angle to the line joining the MW and M31) are indicated in red. The solid black line indicates the median radial velocity profile, and the shaded region indicates the dispersion (defined as 1.4826 times the median absolute deviation) calculating using a bootstrap method. Right-hand panel: the logarithmic slope profile of the median radial velocity. The vertical dashed line indicates the caustic that defines the edge of the Galaxy. This lies at 290 kpc and approximately corresponds to  $0.8 r_{200m}$  (or  $\sim 1.0 r_{\text{vir}}$ ,  $\sim 1.3 r_{200c}$ ), assuming the MW mass estimated by Callingham et al. (2019).

we did previously, the logarithmic slope profile is computed using the fourth-order Savitzky–Golay smoothing algorithm over the 15 nearest bins (Savitzky & Golay 1964). We indicate in the figure dwarfs that are close in angle to the line joining the MW and M31 (i.e.  $|\cos(\theta)| > 0.6$ ). In practice, we find little difference if we include or exclude these dwarfs.

We identify a minimum in the observed population of dwarfs at  $\sim 290$  kpc. Using a bootstrap method to estimate the uncertainty,

we find  $R_{\text{edge}} = 292 \pm 61$  kpc. If we assume the MW halo mass recently measured by Callingham et al. (2019) and a typical halo concentration ( $\sim 10$  for MW-mass haloes; e.g. Neto et al. 2007; Ludlow et al. 2014; Klypin et al. 2016), this radius corresponds to  $0.8 r_{200m}$  (or  $1.3 r_{200c}$ ). Interestingly, this radius (292 kpc) lies at exactly the ‘virial radius’ defined by the fitting formulas in Bryan & Norman (1998). Moreover, this also coincides with the radius where the H I content of LG satellites sharply drops (around 270 kpc; Grcevich & Putman 2009). Given the rather large uncertainty in the measurement, these could simply be coincidences, however, it is worth noting that we are probing an interesting radial regime of the Galactic halo.

We can also use this measured radius to independently estimate the mass of the MW using the escape velocity analysis described by Deason et al. (2019). As mentioned in Section 3.2, this technique depends on the definition of the ‘outer boundary’ of the halo stars. If we use a boundary of 290 kpc, rather than a fixed fraction of  $r_{200c}$  like Deason et al. (2019), we find a mass of  $M_{200c} \sim 1.1 \times 10^{12} M_{\odot}$ . Although there is considerable uncertainty in this definition of halo edge, it is reassuring that this mass is in excellent agreement with the recent measurements by Callingham et al. (2019) and Cautun et al. (2020).

While we suggest that the edge of the MW halo lies at 290 kpc, this remains a tentative result for two important reasons. First, the value is strongly dependent on Leo I (located at 250 kpc): There is a significant gap between the most distant satellite of the MW and the nearest dwarfs in the LG. Secondly, and perhaps most importantly, our census of local dwarfs is far from complete and we have made no attempt to correct for selection effects or observational biases. Indeed, as recently predicted by Fattahi, Navarro & Frenk (2020), there are troves of LG dwarfs waiting to be discovered by future wide-field imaging surveys.

## 4 CONCLUSIONS

In this work, we have analysed three different suites of simulated MW-mass haloes (ELVIS, APOSTLE, and Auriga) to explore the ‘edge’ of Galactic-sized haloes. We use the logarithmic slope profiles of the density and radial velocity distributions to identify the location of caustics in the halo. These features, which correspond to the build up of particles at apocentre, are used to define the edges of the dark matter, stars, and subhalo population. Our main conclusions are summarized as follows:

(i) We typically identify two distinct caustics in the outer dark matter profiles. The outermost caustic, called the ‘splashback’ radius, is the boundary at which accreted dark matter reaches its first orbital apocentre after turnaround. This lies at approximately  $\sim 1.4 r_{200m}$  for MW-mass haloes. We suggest that the second caustic, which is located at a smaller radius ( $\sim 0.6 r_{200m} \approx r_{200c}$ ) and is typically less prominent than the caustic at the splashback radius, corresponds to the edge of the material that has passed through at least two pericentric passages.

(ii) In LG-like environments, the splashback radius of one of the haloes is poorly defined, as it often overlaps with the other halo. However, the second caustic in the dark matter is less affected by the companion and appears to be a more useful choice for the definition of the halo boundary of the MW.

(iii) We identify a prominent caustic in the stellar distribution in both the radial density and velocity profiles. This typically lies at  $0.6 r_{200m}$  and, in the majority of cases, coincides with the second caustic of the dark matter. This feature can potentially be identified

in the MW using future observational facilities, such as LSST and MSE. Moreover, there is scope to measure this edge in external galaxies, either by stacking profiles, or by obtaining deeper and wider images with forthcoming facilities such as the Roman Space Telescope.

(iv) The outer caustic, corresponding to the splashback radius, can be identified in the phase-space distribution of the subhalo population. If we consider only luminous dwarfs (with  $M_{\text{star}} > 10^5 M_{\odot}$ ), the best defined caustic coincides with the second caustic in the dark matter (and hence with the stellar caustic).

(v) We applied our analysis to the currently known population of dwarf galaxies in the LG. We predict that the edge of the MW (defined as the second caustic in the dark matter) lies at  $\sim 290$  kpc. For the total MW-mass measurement by Callingham et al. (2019), this radius coincides approximately with the value of  $r_{\text{vir}}$  obtained from the fitting formula of Bryan & Norman (1998), albeit with significant uncertainty. This is a tentative measurement of the Galactic edge, but will greatly improve with future discoveries of more LG dwarfs.

In many analyses of the MW halo, its outer boundary is a fundamental constraint. Often, the choice is subjective, but as we have argued, it is preferable to define a physically and/or observationally motivated outer edge. Here we have linked the boundary of the underlying dark matter distribution to the observable stellar halo and the dwarf galaxy population. There is great hope that future data will provide a more robust and accurate *measurement* of the edge of the MW and nearby MW-mass galaxies than the one we have presented here. In this work, we have focused on MW-mass haloes in a  $\Lambda$ CDM cosmology, but a similar analysis can be extended to wider mass scales and applied to different cosmologies or dark matter models.

## ACKNOWLEDGEMENTS

AD thanks Andrey Kravtsov for many enlightening science discussions on this topic, and Phil Mansfield for his valuable input. We thank an anonymous referee for improving the clarity of this paper.

AD is supported by a Royal Society University Research Fellowship, and AD, AF, CSF, and KO are supported by the Science and Technology Facilities Council (STFC) (grant numbers ST/F001166/1, ST/I00162X/1, ST/P000541/1). CSF and KO are also supported by ERC Advanced Investigator grant, DMIDAS (GA 786910). This work used the DiRAC Data Centric system at Durham University, operated by the ICC on behalf of the STFC DiRAC HPC Facility ([www.dirac.ac.uk](http://www.dirac.ac.uk)). This equipment was funded by BIS National E-infrastructure capital grant ST/K00042X/1, STFC capital grant ST/H008519/1, and STFC DiRAC Operations grant ST/K003267/1, and Durham University. DiRAC is part of the National E-Infrastructure.

AD thanks the staff at the Durham University Day Nursery who play a key role in enabling research like this to happen.

## DATA AVAILABILITY STATEMENT

The data presented in the figures are available upon request from the corresponding author. The raw simulation data can be requested from the ELVIS (Garrison-Kimmel et al. 2014), APOSTLE (Fattahi et al. 2016; Sawala et al. 2016), and Auriga (Grand et al. 2017) teams.

## REFERENCES

- Adhikari S., Dalal N., Chamberlain R. T., 2014, *J. Cosmol. Astropart. Phys.*, 2014, 019
- Angulo R. E., White S. D. M., 2010, *MNRAS*, 401, 1796
- Ascasibar Y., Hoffman Y., Gottlöber S., 2007, *MNRAS*, 376, 393
- Bahé Y. M., McCarthy I. G., Balogh M. L., Font A. S., 2013, *MNRAS*, 430, 3017
- Balogh M. L., Navarro J. F., Morris S. L., 2000, *ApJ*, 540, 113
- Bauman S. E. et al., 2016, in Hall H. J., Gilmozzi R., Marshall H. K., eds, *Proc. SPIE Conf. Ser. Vol. 9906, Ground-based and Airborne Telescopes VI*. SPIE, Bellingham, p. 990605
- Baxter E. et al., 2017, *ApJ*, 841, 18
- Behroozi P. S., Conroy C., Wechsler R. H., 2010, *ApJ*, 717, 379
- Behroozi P. S., Wechsler R. H., Wu H.-Y., 2013a, *ApJ*, 762, 109
- Behroozi P. S., Wechsler R. H., Wu H.-Y., Busha M. T., Klypin A. A., Primack J. R., 2013b, *ApJ*, 763, 18
- Belokurov V., Sanders J. L., Fattahi A., Smith M. C., Deason A. J., Evans N. W., Grand R. J. J., 2020, *MNRAS*, 494, 3880
- Berlind A. A., Weinberg D. H., 2002, *ApJ*, 575, 587
- Bertschinger E., 1985, *ApJS*, 58, 39
- Binney J., Tremaine S., 2008, *Galactic Dynamics*, 2nd edn. Princeton Univ. Press, Princeton, NJ
- Bochanski J. J., Willman B., Caldwell N., Sanderson R., West A. A., Strader J., Brown W., 2014, *ApJ*, 790, L5
- Boylan-Kolchin M., Bullock J. S., Kaplinghat M., 2011, *MNRAS*, 415, L40
- Bryan G. L., Norman M. L., 1998, *ApJ*, 495, 80
- Bullock J. S., Kolatt T. S., Sigad Y., Somerville R. S., Kravtsov A. V., Klypin A. A., Primack J. R., Dekel A., 2001, *MNRAS*, 321, 559
- Busch P., White S. D. M., 2017, *MNRAS*, 470, 4767
- Callingham T. M. et al., 2019, *MNRAS*, 484, 5453
- Campbell D. J. R. et al., 2017, *MNRAS*, 469, 2335
- Cautun M. et al., 2020, *MNRAS*, 494, 4291
- Chang C. et al., 2018, *ApJ*, 864, 83
- Cohen J. G., Sesar B., Baholzer S., He K., Kulkarni S. R., Prince T. A., Bellm E., Laher R. R., 2017, *ApJ*, 849, 150
- Cole S., Lacey C., 1996, *MNRAS*, 281, 716
- Contigiani O., Hoekstra H., Bahé Y. M., 2019, *MNRAS*, 485, 408
- Cooper A. P. et al., 2010, *MNRAS*, 406, 744
- Crain R. A. et al., 2015, *MNRAS*, 450, 1937
- D'Souza R., Bell E. F., 2018, *MNRAS*, 474, 5300
- Davis M., Efstathiou G., Frenk C. S., White S. D. M., 1985, *ApJ*, 292, 371
- Deason A. J., Belokurov V., Evans N. W., 2011, *MNRAS*, 416, 2903
- Deason A. J. et al., 2012, *MNRAS*, 425, 2840
- Deason A. J., Belokurov V., Evans N. W., Johnston K. V., 2013, *ApJ*, 763, 113
- Deason A., Wetzel A., Garrison-Kimmel S., 2014a, *ApJ*, 794, 115
- Deason A. J., Belokurov V., Koposov S. E., Rockosi C. M., 2014b, *ApJ*, 787, 30
- Deason A. J., Mao Y.-Y., Wechsler R. H., 2016, *ApJ*, 821, 5
- Deason A. J., Belokurov V., Koposov S. E., Gómez F. A., Grand R. J., Marinacci F., Pakmor R., 2017, *MNRAS*, 470, 1259
- Deason A. J., Belokurov V., Koposov S. E., Lancaster L., 2018, *ApJ*, 862, L1
- Deason A. J., Fattahi A., Belokurov V., Evans N. W., Grand R. J. J., Marinacci F., Pakmor R., 2019, *MNRAS*, 485, 3514
- Diemand J., Kuhlen M., 2008, *ApJ*, 680, L25
- Diemand J., Kuhlen M., Madau P., 2007, *ApJ*, 667, 859
- Diemer B., Kravtsov A. V., 2014, *ApJ*, 789, 1
- Diemer B., More S., Kravtsov A. V., 2013, *ApJ*, 766, 25
- Diemer B., Mansfield P., Kravtsov A. V., More S., 2017, *ApJ*, 843, 140
- Eke V. R., Navarro J. F., Frenk C. S., 1998, *ApJ*, 503, 569
- Fattahi A. et al., 2016, *MNRAS*, 457, 844
- Fattahi A., Navarro J. F., Frenk C. S., Oman K. A., Sawala T., Schaller M., 2018, *MNRAS*, 476, 3816
- Fattahi A. et al., 2019, *MNRAS*, 484, 4471
- Fattahi A., Navarro J. F., Frenk C. S., 2020, *MNRAS*, 493, 2596
- Fillmore J. A., Goldreich P., 1984, *ApJ*, 281, 1

- Frenk C. S., White S. D. M., Davis M., Efstathiou G., 1988, *ApJ*, 327, 507  
 Garrison-Kimmel S., Boylan-Kolchin M., Bullock J. S., Lee K., 2014, *MNRAS*, 438, 2578  
 Garrison-Kimmel S., Bullock J. S., Boylan-Kolchin M., Bardwell E., 2017, *MNRAS*, 464, 3108  
 Genel S., Bouché N., Naab T., Sternberg A., Genzel R., 2010, *ApJ*, 719, 229  
 Genina A. et al., 2018, *MNRAS*, 474, 1398  
 Genina A. et al., 2019, preprint ([arXiv:1911.09124](https://arxiv.org/abs/1911.09124))  
 Gill S. P. D., Knebe A., Gibson B. K., 2005, *MNRAS*, 356, 1327  
 Grand R. J. J. et al., 2016, *MNRAS*, 460, L94  
 Grand R. J. J. et al., 2017, *MNRAS*, 467, 179  
 Grand R. J. J. et al., 2018, *MNRAS*, 474, 3629  
 Grand R. J. J., Deason A. J., White S. D. M., Simpson C. M., Gómez F. A., Marinacci F., Pakmor R., 2019a, *MNRAS*, 487, L72  
 Grand R. J. J. et al., 2019b, *MNRAS*, 490, 4786  
 Grevech J., Putman M. E., 2009, *ApJ*, 696, 385  
 Gunn J. E., Gott J., Richard I., 1972, *ApJ*, 176, 1  
 Harmsen B., Monachesi A., Bell E. F., de Jong R. S., Bailin J., Radburn-Smith D. J., Holwerda B. W., 2017, *MNRAS*, 466, 1491  
 Hayashi E., White S. D. M., 2008, *MNRAS*, 388, 2  
 Hernitschek N. et al., 2018, *ApJ*, 859, 31  
 Ivezić Ž. et al., 2019, *ApJ*, 873, 111  
 Jenkins A., 2013, *MNRAS*, 434, 2094  
 Klypin A., Yepes G., Gottlöber S., Prada F., Heß S., 2016, *MNRAS*, 457, 4340  
 Knebe A. et al., 2011, *MNRAS*, 415, 2293  
 Komatsu E. et al., 2011, *ApJS*, 192, 18  
 Kravtsov A. V., 2013, *ApJ*, 873, L31  
 Kravtsov A. V., Berlind A. A., Wechsler R. H., Klypin A. A., Gottlöber S., Allgood B. o., Primack J. R., 2004, *ApJ*, 609, 35  
 Lahav O., Lilje P. B., Primack J. R., Rees M. J., 1991, *MNRAS*, 251, 128  
 Larson D. et al., 2011, *ApJS*, 192, 16  
 Leonard P. J. T., Tremaine S., 1990, *ApJ*, 353, 486  
 Lovell M. R. et al., 2017, *MNRAS*, 468, 4285  
 Ludlow A. D., Navarro J. F., Springel V., Jenkins A., Frenk C. S., Helmi A., 2009, *ApJ*, 692, 931  
 Ludlow A. D., Navarro J. F., Springel V., Vogelsberger M., Wang J., White S. D. M., Jenkins A., Frenk C. S., 2010, *MNRAS*, 406, 137  
 Ludlow A. D., Navarro J. F., Angulo R. E., Boylan-Kolchin M., Springel V., Frenk C., White S. D. M., 2014, *MNRAS*, 441, 378  
 McConnachie A. W., 2012, *AJ*, 144, 4  
 Mamon G. A., Sanchis T., Salvador-Solé E., Solanes J. M., 2004, *A&A*, 414, 445  
 Mansfield P., Kravtsov A. V., Diemer B., 2017, *ApJ*, 841, 34  
 Marinacci F., Grand R. J. J., Pakmor R., Springel V., Gómez F. A., Frenk C. S., White S. D. M., 2017, *MNRAS*, 466, 3859  
 Mauron N., Azzopardi M., Gigoyan K., Kendall T. R., 2004, *A&A*, 418, 77  
 Merritt A., van Dokkum P., Abraham R., Zhang J., 2016, *ApJ*, 830, 62  
 Monachesi A., Gómez F. A., Grand R. J. J., Kauffmann G., Marinacci F., Pakmor R., Springel V., Frenk C. S., 2016, *MNRAS*, 459, L46  
 Monachesi A. et al., 2019, *MNRAS*, 485, 2589  
 Moore B., Ghigna S., Governato F., Lake G., Quinn T., Stadel J., Tozzi P., 1999a, *ApJ*, 524, L19  
 Moore B., Quinn T., Governato F., Stadel J., Lake G., 1999b, *MNRAS*, 310, 1147  
 More S., Diemer B., Kravtsov A. V., 2015, *ApJ*, 810, 36  
 More S. et al., 2016, *ApJ*, 825, 39  
 Moster B. P., Somerville R. S., Maulbetsch C., van den Bosch F. C., Macciò A. V., Naab T., Oser L., 2010, *ApJ*, 710, 903  
 Murata R., Sunayama T., Oguri M., More S., Nishizawa A. J., Nishimichi T., Osato K., 2020, preprint ([arXiv:2001.01160](https://arxiv.org/abs/2001.01160))  
 Navarro J. F., Frenk C. S., White S. D. M., 1996, *ApJ*, 462, 563  
 Navarro J. F., Frenk C. S., White S. D. M., 1997, *ApJ*, 490, 493  
 Neto A. F. et al., 2007, *MNRAS*, 381, 1450  
 Pawlowski M. S., Ibata R. A., Bullock J. S., 2017, *ApJ*, 850, 132  
 Peñarrubia J., Navarro J. F., McConnachie A. W., 2008, *ApJ*, 673, 226  
 Planck Collaboration et al., 2014, *A&A*, 571, A16  
 Prada F., Klypin A. A., Simonneau E., Betancort-Rijo J., Patiri S., Gottlöber S., Sanchez-Conde M. A., 2006, *ApJ*, 645, 1001  
 Purcell C. W., Bullock J. S., Zentner A. R., 2007, *ApJ*, 666, 20  
 Read J. I., Iorio G., Agertz O., Fraternali F., 2017, *MNRAS*, 467, 2019  
 Sales L. V., Navarro J. F., Abadi M. G., Steinmetz M., 2007, *MNRAS*, 379, 1475  
 Savitzky A., Golay M. J. E., 1964, *Anal. Chem.*, 36, 1627  
 Sawala T. et al., 2015, *MNRAS*, 448, 2941  
 Sawala T. et al., 2016, *MNRAS*, 457, 1931  
 Sawala T., Pihajoki P., Johansson P. H., Frenk C. S., Navarro J. F., Oman K. A., White S. D. M., 2017, *MNRAS*, 467, 4383  
 Schaye J. et al., 2015, *MNRAS*, 446, 521  
 Schönrich R., Binney J., Dehnen W., 2010, *MNRAS*, 403, 1829  
 Sesar B., Jurić M., Ivezić Ž., 2011, *ApJ*, 731, 4  
 Shin T. et al., 2019, *MNRAS*, 487, 2900  
 Shull J. M., 2014, *ApJ*, 784, 142  
 Simpson C. M., Grand R. J. J., Gómez F. A., Marinacci F., Pakmor R., Springel V., Campbell D. J. R., Frenk C. S., 2018, *MNRAS*, 478, 548  
 Slater C. T., Nidever D. L., Munn J. A., Bell E. F., Majewski S. R., 2016, *ApJ*, 832, 206  
 Spergel D. et al., 2015, preprint ([arXiv:1503.03757](https://arxiv.org/abs/1503.03757))  
 Springel V., 2005, *MNRAS*, 364, 1105  
 Springel V., White S. D. M., Tormen G., Kauffmann G., 2001, *MNRAS*, 328, 726  
 Springel V. et al., 2008, *MNRAS*, 391, 1685  
 Stadel J., Potter D., Moore B., Diemand J., Madau P., Zemp M., Kuhlen M., Quilis V., 2009, *MNRAS*, 398, L21  
 Starkenburg E., Oman K. A., Navarro J. F., Crain R. A., Fattahi A., Frenk C. S., Sawala T., Schaye J., 2017, *MNRAS*, 465, 2212  
 Takada M. et al., 2014, *PASJ*, 66, R1  
 Teyssier M., Johnston K. V., Kuhlen M., 2012, *MNRAS*, 426, 1808  
 Wang J. et al., 2011, *MNRAS*, 413, 1373  
 Wechsler R. H., Tinker J. L., 2018, *ARA&A*, 56, 435  
 Wechsler R. H., Bullock J. S., Primack J. R., Kravtsov A. V., Dekel A., 2002, *ApJ*, 568, 52  
 Wetzel A. R., Tinker J. L., Conroy C., van den Bosch F. C., 2014, *MNRAS*, 439, 2687  
 Wetzel A. R., Deason A. J., Garrison-Kimmel S., 2015, *ApJ*, 807, 49  
 Xhakaj E., Diemer B., Leauthaud A., Wasserman A., Huang S., Luo Y., Adhikari S., Singh S., 2019, preprint ([arXiv:1911.09295](https://arxiv.org/abs/1911.09295))  
 Xue X.-X., Rix H.-W., Ma Z., Morrison H., Bovy J., Sesar B., Janesh W., 2015, *ApJ*, 809, 144  
 Zavala J., Okamoto T., Frenk C. S., 2008, *MNRAS*, 387, 364  
 Zürcher D., More S., 2019, *ApJ*, 874, 184

This paper has been typeset from a  $\text{\TeX}/\text{\LaTeX}$  file prepared by the author.